RSC Advances

ROYAL SOCIETY OF CHEMISTRY

PAPER

View Article Online
View Journal | View Issue

Check for updates

Cite this: *RSC Adv.*, 2021, **11**, 9746

Enhanced photocatalytic performance of rhodamine B and enrofloxacin by Pt loaded $Bi_4V_2O_{11}$: boosted separation of charge carriers, additional superoxide radical production, and the photocatalytic mechanism†

Yanjun Zhao,[a] Xintong Liu,[b] Shaonan Gu[c] and Jiemin Liu *[a]

Received 4th January 2021
Accepted 19th February 2021

DOI: 10.1039/d1ra00055a

rsc.li/rsc-advances

Photocatalytic performance is influenced by two contradictory factors, which are light absorption range and separation of charge carriers. Loading noble metals with nanosized interfacial contact is expected to improve the separation and transfer of photo-excited charge carriers while enlarging the light absorption range of the semiconductor photocatalyst. Therefore, it should be possible to improve the photocatalytic performance of pristine nontypical stoichiometric semiconductor photocatalysts by loading a specific noble metal. Herein, a series of novel Pt–$Bi_4V_2O_{11}$ photocatalysts have been successfully prepared *via* a surface reduction technique. The crystal structure, morphology, and photocatalytic performance, as well as photo-electron properties of the as-synthesized samples were fully characterized. Moreover, the series of Pt–$Bi_4V_2O_{11}$ samples were evaluated to remove typical organic pollutants, rhodamine B and enrofloxacin, from aqueous solutions. The photoluminescence, quenching experiments and the electron spin resonance technique were utilized to identify the effective radicals during the photocatalytic process and understand the photocatalytic mechanism. The photocatalytic performance of Pt–$Bi_4V_2O_{11}$ was tremendously enhanced compared with pristine $Bi_4V_2O_{11}$, and there was additional $^{\bullet}O^{2-}$ produced during the photocatalytic process. This study deeply investigated the relation between the separation of charge carriers and the light harvesting, and revealed a promising strategy for fabricating efficient photocatalysts for both dyes and antibiotics.

1. Introduction

Organic dyes and antibiotics are closely related to human society due to their wide field of application.[1,2] However, their emission into aquatic ecosystems poses severe threats to environment, and causes detrimental effects on human health as well. For example, rhodamine B (RhB) is a widely used cationic dye in textiles, dyeing, and leather industries and biomedical laboratories.[3] However, RhB is also toxic and carcinogenic for humans and animals.[4,5] In addition, enrofloxacin (ENR) is a common fluoroquinolone antibiotic, which is widely used in veterinary and human medicine as well as a feed additive in animal husbandry. However, the residual ENR in environment can promote antibiotic-resistance of bacteria and cause potential threats to ecosystems and human health.[6,7] Although the hazards of organic dyes and antibiotics were different, the degradation of them was difficult because of their complex and stable structures. Thus, the development of effective and environmentally friendly methods to degrade these organic pollutants became significant and necessary.

Among the various water treatment methods, semiconductor photocatalysis is considered as a green and promising alternative to remove organic pollutants from aqueous solutions due to its environmental friendliness and high efficiency.[8–10] It is known that light absorption range and separation of charge carriers are two decisive factors in the photocatalytic process.[11,12] However, these two factors are contradictory: enlarging the light absorption range requires narrowing down the band gap, but the narrowed band gap may promote the recombination of charge carriers.[13] Therefore, one of the main emphasis in semiconductor photocatalysis is to improve the light absorption capacities of the photocatalysts while facilitate the separation of charge carriers.[14–16]

---

[a] *School of Chemistry and Biological Engineering, University of Science and Technology Beijing, No. 30 Xueyuan Road, Haidian District, Beijing 100083, People's Republic of China. E-mail: liujm@ustb.edu.cn; Fax: +86-10-6233-2281; Tel: +86-10-8237-6678*

[b] *School of Light Industry, Beijing Technology and Business University, No. 33 Fucheng Road, Haidian District, Beijing 100048, People's Republic of China*

[c] *Key Laboratory of Fine Chemicals in Universities of Shandong, School of Chemistry and Pharmaceutical Engineering, Qilu University of Technology, Shandong Academy of Sciences, No. 3501 Daxue Road, Changqing District, Jinan 250353, Shandong Province, People's Republic of China*

† Electronic supplementary information (ESI) available. See DOI: 10.1039/d1ra00055a

Compared with typical stoichiometric semiconductor photocatalysts, the corresponding nontypical stoichiometric semiconductor photocatalysts showed great potential in photocatalysis due to their distinct band structures, efficient separation and mobility of photogenerated charge carriers.[17] Therefore, otherwise than typical stoichiometric semiconductors, the nontypical stoichiometric semiconductors were also ideal candidates as efficient photocatalysts to remove organic pollutants, such as $W_{18}O_{49}$,[18,19] Bi_3O_4Cl,[20] $Bi_2VO_{5.5}$,[21] Bi_5O_7I,[22] $Bi_{24}O_{31}Cl_{10}$,[23,24] $Bi_{24}O_{31}Br_{10}$,[25,26] $Bi_4V_2O_{11}$.[27,28] Among these nontypical stoichiometric semiconductor photocatalysts, $Bi_4V_2O_{11}$ has attracted continuous attentions because of the consistent element composition and similar crystal structure relative to $BiVO_4$.[29] Moreover, the light absorption range of $Bi_4V_2O_{11}$ is much larger than that of $BiVO_4$. However, the recombination of charge carriers of $Bi_4V_2O_{11}$ is also much higher than that of $BiVO_4$, which restricted its photocatalytic performance. Notably, promoting the separation of charge carriers is essential for enhancing the photocatalytic performance of $Bi_4V_2O_{11}$. In addition, due to the limitation of energy band potential, $Bi_4V_2O_{11}$ could only produce specific radicals during the process of photocatalytic.[30] Hence, the induction of $Bi_4V_2O_{11}$ for producing additional radicals is also beneficial for enhancing the photocatalytic performance.[31]

Loading noble metals with nanosized interfacial contact was one of the effective methods to improve the separation and transportation of photo-excited charge carriers, which resulted from the favorable interfacial contact and short transfer pathway.[32–34] Besides, some noble metals could also enlarge the light absorption range of the semiconductor photocatalyst.[35,36] Recently, several novel noble metal loaded visible light driven photocatalysts have been reported to show enhanced catalytic performance.[37–39] Besides, loading noble metal might also produce some additional superoxide radicals by directly utilizing the photogenerated electrons.[31] Hence, it is of great importance to employ appropriate noble metal on the surface of the $Bi_4V_2O_{11}$ to enhance the photocatalytic performance.

Therefore, in this paper, novel Pt loaded $Bi_4V_2O_{11}$ catalysts were successfully prepared *via* a surface reduction method, and were evaluated as photocatalysts to degrade typical organic dyes and antibiotics, namely rhodamine B (RhB) and enrofloxacin (ENR). The photocatalytic experiments illustrated that the photocatalytic performance of Pt–$Bi_4V_2O_{11}$ was tremendously enhanced. The photoluminescence (PL) and quenching experiments results demonstrated that the improvement of photocatalytic performance could mainly attributed to the rapid transmission of photo-excited charge carriers and the additional production of superoxide radicals. This study not only provided a promising strategy for fabricating efficient photocatalysts for organic dyes and antibiotics, but also carried forward the photocatalytic theory.

2. Experimental

2.1. Synthesis of samples

The chemicals used in this work were supplied by Sinopharm Chemical Reagent Corporation (Shanghai, China), and the chemicals were of analytical grade. The preparation of $Bi_4V_2O_{11}$ photocatalyst was through one-pot facile solvothermal method.[40] First, 70 mL ethylene glycol (EG) was used to dissolve 1 g urea and 2.43 g $Bi(NO_3)_3 \cdot 5H_2O$ under vigorous stirring. Then 0.30 g $NaVO_3$ was added, and the pH of the above mixture was modulated to about 7.5 by adding diluent ammonia. Subsequently, the as-prepared precursor suspension was added into a 100 mL Teflon-lined stainless autoclave and kept at 478 K for 24 h. Afterwards, the reactor was cool naturally. Afterwards, the prepared $Bi_4V_2O_{11}$ was first washed with ultra-pure water three times then washed with ethanol three times. Finally, $Bi_4V_2O_{11}$ was dried in an oven at 373 K for 10 h.

The preparation method of 2%, 4%, 6%, and 8% Pt loaded $Bi_4V_2O_{11}$ samples (where 2%, 4%, 6% and 8% are the atomic ratio of Pt/Bi) was described as follows. 0.5 mmol as-synthesized pure $Bi_4V_2O_{11}$ was added into the certain amount of H_2PtCl_6 solutions under ultrasonic-assistance for 1 h. Next, the sample was dried for 12 h at 373 K and cooled naturally. Then the obtained sample was impregnated within 30 mL methanol by ultrasonication, and the obtained dark brown suspension was stirred for another 1 h. At last, the suspension was centrifuged, and washed by ultra-pure water and ethanol, then the synthesized Pt loaded $Bi_4V_2O_{11}$ was dried at 333 K for 10 h.

2.2. Characterization of the photocatalysts

The crystal structure of pure $Bi_4V_2O_{11}$ and Pt–$Bi_4V_2O_{11}$ series samples were examined by X-ray diffraction (XRD) (D/MAX-RB; Rigaku, Japan). Scanning electron microscopy (SEM) (S-4800; Hitachi, Japan) was used to investigate the surface morphologies of the as-synthesized photocatalysts. Transmission electron microscope (F-20, FEI; USA) was examined to further identify the formation of Pt–$Bi_4V_2O_{11}$. The Brunauer–Emmett–Teller (BET) surface areas were determined using an automatic volumetric sorption analyzer (Micromeritics model ASAP 2000) at 77 K. Moreover, the UV-Vis diffuse reflectance spectra (DRS) of the as-synthesized photocatalysts were determined by a T9s UV-Vis spectrophotometer (Persee, China). Besides, the X-ray photoelectron spectroscopies (XPS) of Pt–$Bi_4V_2O_{11}$ were analyzed by an ESCALAB 250Xi X-ray photoelectron spectrometer (Thermo, USA). A Bruker A300 spectrometer (Bruker, Germany) was used to identify the main radicals during the photocatalytic process.

2.3. Photocatalytic performances studies

The degradations of 20 mmol L^{-1} RhB solution under visible light illumination were evaluated to investigate the photocatalytic performances of $Bi_4V_2O_{11}$ and Pt–$Bi_4V_2O_{11}$ series samples. Moreover, the degradation of 40 mg L^{-1} ENR solution using the optimal sample was also conducted to study the potential of the as-prepared photocatalyst for antibiotics removal. A 400 W Xe lamp with a UV-cut-off filter ($\lambda > 420$ nm) was fixed at 10 cm from the samples to simulate the light source. The photocatalytic experiments were carried out by adding 40 mg of the studied photocatalysts into 40 mL RhB or ENR solutions. The RhB or ENR solutions with the photocatalysts samples were stirred in dark for 2 h to reach the adsorption–desorption equilibrium before light illumination. For RhB, the aqueous samples were taken at 0.5 h intervals, while for ENR, the samples were taken at 1 h intervals. The absorbance spectrum of RhB at 553 nm and the UV-Vis spectra of ENR were determined by a UV-Vis spectrophotometer. The degradation efficiencies were evaluated by C/C_0, where C_0 (mmol L^{-1}) was the initial concentration of RhB or ENR, and C (mmol L^{-1}) is the concentration of RhB or ENR at a certain time.

3. Result and discussion

3.1. XRD analysis

The XRD patterns of $Bi_4V_2O_{11}$ and Pt–$Bi_4V_2O_{11}$ series samples were presented in Fig. 1. For pure $Bi_4V_2O_{11}$, the diffraction peaks were consistent with the standard data for orthorhombic crystal structure of $Bi_4V_2O_{11}$ (JCPDS No. 42-135),[27] and no impurity peaks were detected, which indicated the high purity of $Bi_4V_2O_{11}$. As for Pt–$Bi_4V_2O_{11}$ series samples, the XRD patterns of both the $Bi_4V_2O_{11}$ and elemental Pt phases were detected, and the characteristic peaks have been labeled respectively. The peaks at 10.9° and 28.3° were attributed to the orthorhombic $Bi_4V_2O_{11}$, while the distinctive peak at 18.8° was attributed to the elemental Pt (JCPDS No. 04-802).[41] Notably, with the increase of Pt contents, the intensity of peak of Pt was gradually enhanced, which confirmed the formation of Pt on the crystal surface of $Bi_4V_2O_{11}$. However, other Pt peaks was hard to observe, which might be caused by the high dispersion and low content of Pt in Pt–$Bi_4V_2O_{11}$ series samples. Besides, the intensities of the peaks stand for $Bi_4V_2O_{11}$ decreased, which indicated the coupling of the Pt on the surface of $Bi_4V_2O_{11}$.

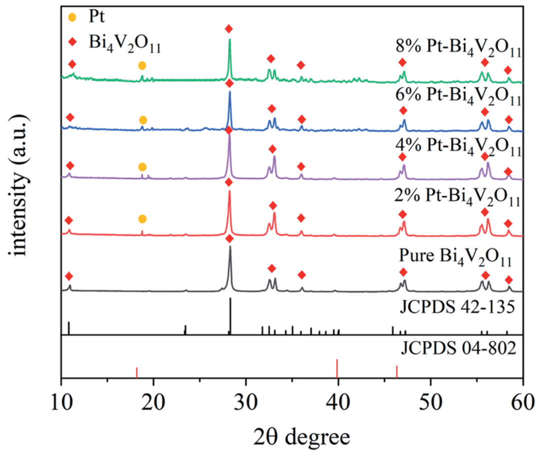

Fig. 1 XRD patterns of the pure $Bi_4V_2O_{11}$, and Pt loaded $Bi_4V_2O_{11}$ samples.

3.2. Morphology characterization

SEM images of $Bi_4V_2O_{11}$ and Pt–$Bi_4V_2O_{11}$ series samples were depicted in Fig. 2. As shown in Fig. 2A, pure $Bi_4V_2O_{11}$ exhibited irregular polygon grains agglomerated in a disordered manner. As shown in Fig. 2B–E, the morphologies of Pt–$Bi_4V_2O_{11}$ series samples showed Pt particles dispersed on $Bi_4V_2O_{11}$ surface uniformly. Notably, with the increase of the Pt contents, more Pt nanoparticles were observed on $Bi_4V_2O_{11}$ surface. Furthermore, in order to observe the distribution of Pt nanoparticles and compare the different Pt loading contents, EDS mapping of Pt–$Bi_4V_2O_{11}$ series samples were determined and shown in Fig. S1.† As observed in Fig. S1,† Pt nanoparticles were uniformly dispersed on $Bi_4V_2O_{11}$ surface. Besides, with the increase of Pt contents, more Pt nanoparticles were observed, and the sizes of Pt particle were enlarged clearly. Moreover, the loading contents were consistent with the theoretical values. The results of EDS mapping also revealed that Pt were successfully loaded on the surface of $Bi_4V_2O_{11}$.

Moreover, the TEM and HRTEM of pristine $Bi_4V_2O_{11}$ and 6% Pt–$Bi_4V_2O_{11}$ composite samples were determined and illustrated in Fig. 3. As shown in Fig. 3A, it can be clearly observed that pristine $Bi_4V_2O_{11}$ possess the irregular polygon grain morphology. Moreover, the 0.306 lattice fringe observed in Fig. 3B was attributed to the (0 2 0) plane of pristine $Bi_4V_2O_{11}$. As shown in Fig. 3C, TEM image of the 6% Pt–$Bi_4V_2O_{11}$ sample also showed irregular polygon morphology, which was consistent with the results of SEM studies. The HRTEM image showed in Fig. 3D could further investigate the growth of Pt on the surface of the $Bi_4V_2O_{11}$ bulk, and the lattice fringe of (1 3 1) plane of $Bi_4V_2O_{11}$ bulk was 0.176 nm, while the lattice fringe of Pt (2 0 0) was 0.195 nm. The results of TEM and HRTEM strongly proved the formation of Pt–$Bi_4V_2O_{11}$ systems.

In order to gain further insights into the surface properties of the as-prepared photocatalysts, the surface areas of $Bi_4V_2O_{11}$ and Pt–$Bi_4V_2O_{11}$ were analyzed. The nitrogen adsorption–desorption isotherms of the as-prepared samples were shown in Fig. S2,† and the BET surface areas and N_2 sorption capacities were shown in Table S1.† The N_2 adsorption–desorption isotherms of all the as-prepared photocatalysts were categorized as type IV. Besides, with the increase of Pt loading content, the BET surface areas of Pt–$Bi_4V_2O_{11}$ increased until the Pt content reached 4%. When the Pt loading content higher than 4%, the surface areas showed a dramatically decrease. This phenomenon might be due to that when the loading content was low, the size of loaded Pt was small, which led to the increase of surface areas. However, with the increase of loading content, the size of loaded Pt would increase, which might wrap the original surface and cause the decrease of surface area.

3.3. Chemical state analysis

Moreover, in order to investigate the elemental compositions and surface chemical states of Pt loaded $Bi_4V_2O_{11}$ and pristine $Bi_4V_2O_{11}$ samples, the XPS spectra of 6% Pt–$Bi_4V_2O_{11}$ and pristine $Bi_4V_2O_{11}$ were determined, and the deconvolution spectra of Bi 4f, O 1s, V 2p and Pt 4f were shown in Fig. 4A–D, respectively. Before analyzing, all peaks were calibrated according to the standard C 1s signal at 284.8 eV. The synthesis of Pt–$Bi_4V_2O_{11}$ involved nitrogen atoms, however, there is no peak detected corresponding to nitrogen at approximately 400 eV,[42] which indicated that there is no nitrogen doping on the Pt–$Bi_4V_2O_{11}$ sample. As depicted in Fig. 4A–C, the peaks of Bi 4f, O 1s and V 2p of 6% Pt–$Bi_4V_2O_{11}$ showed slightly shift in comparison of pristine $Bi_4V_2O_{11}$, which might be due to the

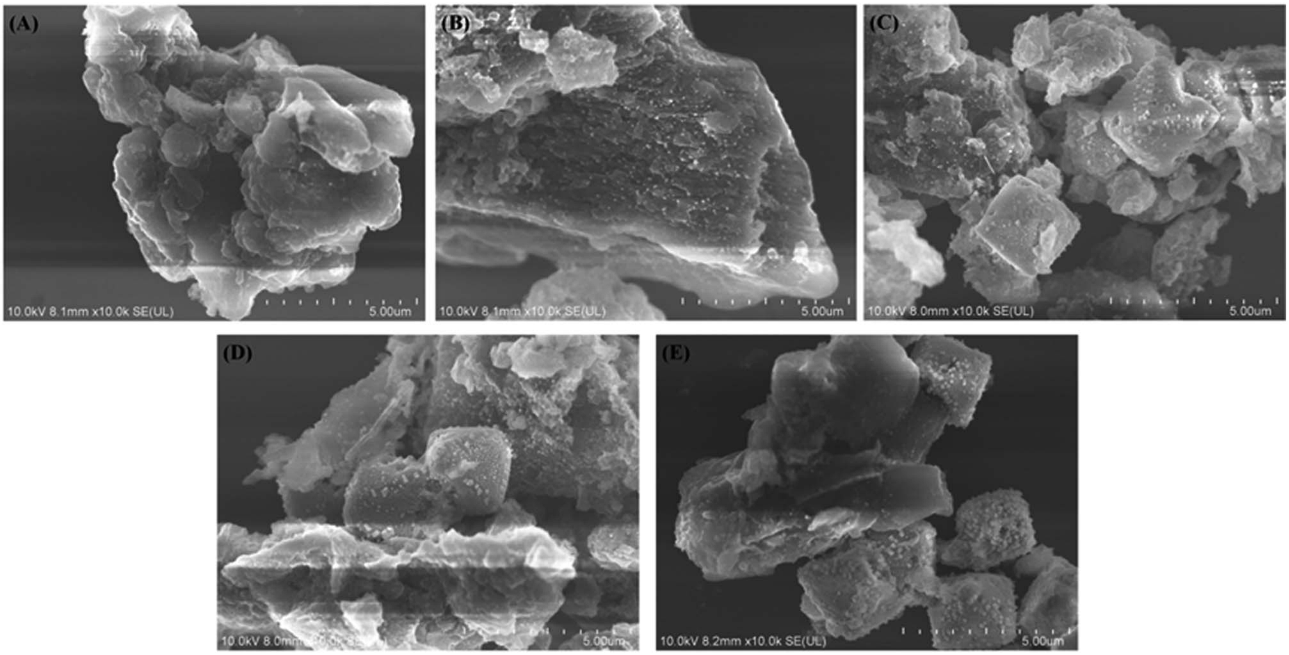

Fig. 2 SEM images of $Bi_4V_2O_{11}$ (A) and Pt–$Bi_4V_2O_{11}$ series samples with Pt contents from 2% to 8% (B–E).

interaction between $Bi_4V_2O_{11}$ and metallic Pt.[43] Moreover, there was a characteristic peak in the deconvolution spectrum of Pt 4f (71.4 eV) at 6% Pt–$Bi_4V_2O_{11}$ in Fig. 4D, which was not observed in pristine $Bi_4V_2O_{11}$. This result indicated Pt was successfully attached on the surface of $Bi_4V_2O_{11}$.[44] Overall, the results of XPS analysis confirmed the successful synthesis of Pt loaded $Bi_4V_2O_{11}$ samples.

3.4. Optical properties

The optical properties of the $Bi_4V_2O_{11}$ and Pt–$Bi_4V_2O_{11}$ series samples at 500–700 nm were studied by UV-Vis DRS, and the results were shown in Fig. 5. It can be clearly observed that compared with pure $Bi_4V_2O_{11}$, the light absorption range of Pt–$Bi_4V_2O_{11}$ were enlarged after Pt loading, which could react to visible light illumination. Among the as-prepared samples, 8% Pt–$Bi_4V_2O_{11}$ had the largest absorption range, while pure $Bi_4V_2O_{11}$ had a relatively narrow absorption range. The red shift of the composite sample is obvious, which indicates that the addition of noble metal platinum can improve the optometric absorption of the material, and for 8% Pt–$Bi_4V_2O_{11}$, the absorption range is the largest in the composite sample.

Furthermore, the band gap energies (E_g) of semiconductor photocatalysts were calculated according to the following equation:[45]

$$Ah\nu = \alpha(h\nu - E_g)^{n/2}$$

where A is the absorption coefficient, h stands for the Planck's constant, ν is the light frequency, α is the proportionality constant, respectively. The type of transition determined the value of constant n. Due to the band gap of $Bi_4V_2O_{11}$ was indirect, the value of n was 4.[46]

Accordingly, the band gap energy (E_g) of the pure $Bi_4V_2O_{11}$ was calculated to be 2.10 eV. As for Pt–$Bi_4V_2O_{11}$ series samples, E_g were calculated to be 2.08, 2.02, 1.95 and 1.91 eV respectively for the Pt contents from 2% to 8%. The results demonstrated that loading Pt narrowed the band gap of $Bi_4V_2O_{11}$, and with the increase of Pt content, E_g of Pt–$Bi_4V_2O_{11}$ showed a tendency of decrease.[47]

3.5. Photocatalytic properties

The photodegradation performances of the as-prepared samples for RhB under visible light illumination were evaluated. In order to avoid the effect of adsorption,[48] the samples were dispersed in RhB solution and continuously stirred in dark for 2 h to ensure the samples reached the adsorption–desorption equilibrium. Before analysis, the adsorption capacities were deducted.

As presented in Fig. 6A, the photocatalytic activity of pristine $Bi_4V_2O_{11}$ is relatively low, and after 150 min of visible light irradiation, RhB concentration showed no significant change. The poor photocatalytic activity may be due to the rapid recombination of carriers. The photocatalytic activity of Pt–$Bi_4V_2O_{11}$ composite samples was enhanced, the decomposition rates enhanced with the increase of Pt content until it reached 6%. As Fig. 6A shown, for 6% Pt–$Bi_4V_2O_{11}$ samples, the degradation rate of RhB after irradiation for 150 min reached about 98%. However, when Pt content was further increased to 8%, photocatalytic activity declined, possibly due to excessive Pt coverage that further narrowed the band gap and inhibited carrier separation.[49,50]

Moreover, other than organic dye RhB, pristine $Bi_4V_2O_{11}$ and the superior catalyst (6% Pt–$Bi_4V_2O_{11}$) was used to degrade colorless enrofloxacin (ENR). We found that pristine $Bi_4V_2O_{11}$

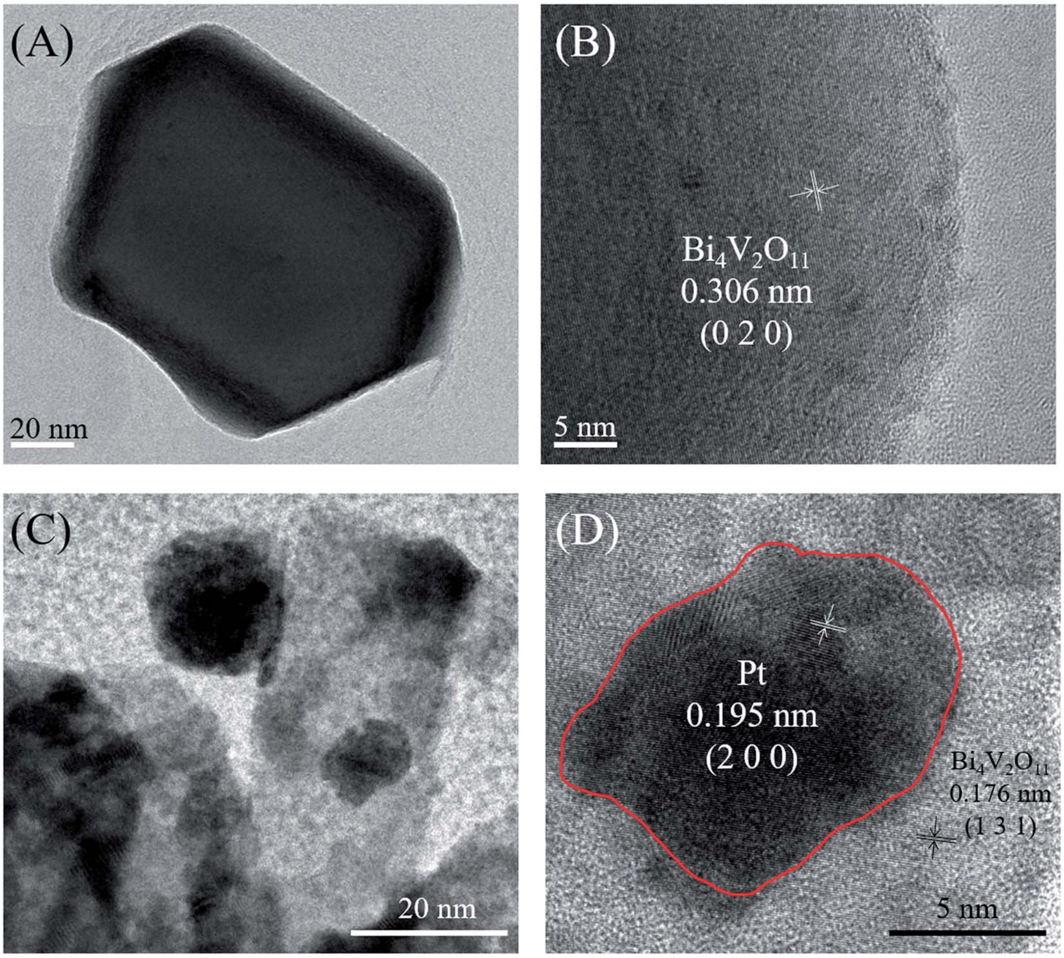

Fig. 3 TEM image pristine $Bi_4V_2O_{11}$ (A), HRTEM image of pristine $Bi_4V_2O_{11}$ (B), TEM image of 6% Pt–$Bi_4V_2O_{11}$ sample (C), and HRTEM image of 6% Pt–$Bi_4V_2O_{11}$ sample (D).

sample showed no obvious degradation efficiency for ENR, while as shown in Fig. 6B, it can be observed that after 4 h visible light illumination, almost 50% enrofloxacin has been efficiently degraded by 6% Pt–$Bi_4V_2O_{11}$. The above results suggested that Pt–$Bi_4V_2O_{11}$ could be a promising strategy for ENR degradation. Furthermore, the degradation rates under pH values ranging from 4.0 to 9.0 were also evaluated. However, the results showed that the effect of solution pH was mainly reflected in the adsorption process, which was deducted in the discussion of photocatalytic properties. Therefore, the photocatalytic performances showed no obvious change under the studied pH conditions.[51]

The stability of the prepared photocatalysts strongly affects its practical application potential.[52] The photocatalytic stability of 6% Pt–$Bi_4V_2O_{11}$ was confirmed by four cyclic photodegradation of RhB. For comparing, the stability of pristine sample has been tested as well. As revealed in Fig. 6C, no significant inactivation of pristine $Bi_4V_2O_{11}$ and 6% Pt–$Bi_4V_2O_{11}$ photocatalyst were found, and the degradation rate of 6% Pt–$Bi_4V_2O_{11}$ was still superior over pristine $Bi_4V_2O_{11}$ after 4 cyclic experiments. Moreover, the cyclic photodegradation of ENR by 6% Pt–$Bi_4V_2O_{11}$ was also investigated, and the results were shown in Fig. 6D. After 4 cyclic experiments, the degradation rate of ENR remained at 45%, which also confirmed the stability of 6% Pt–$Bi_4V_2O_{11}$. Therefore, the 6% Pt–$Bi_4V_2O_{11}$ photocatalyst shows excellent stability to become a promising photocatalysts for regulating organic pollutants.

3.6. Photocatalytic mechanism

To summarize, compared with pristine $Bi_4V_2O_{11}$, the Pt–$Bi_4V_2O_{11}$ series samples showed highly enhanced photocatalytic properties. Photoluminescence (PL) spectra were utilized to verify the effective inhibition of charge carriers recombination by loading elemental Pt on the substrate surface of $Bi_4V_2O_{11}$.[53]

As shown in Fig. 7A, the photoluminescence signal at about 367 nm was contributed to the electron–hole pairs formed on the $Bi_4V_2O_{11}$ substrate.[54] In general, a lower PL intensity suggests a better electron transfer efficiency, which enhances photocatalytic activity.[55] We also observed that compared with pure $Bi_4V_2O_{11}$, the photoluminescence intensity of Pt–$Bi_4V_2O_{11}$ series samples decreased significantly, indicating that the separation rate of photogenic charge carriers was tremendously enhanced. In particular, for 6% Pt–$Bi_4V_2O_{11}$ samples, the loaded Pt effectively transmitted electrons, improving the

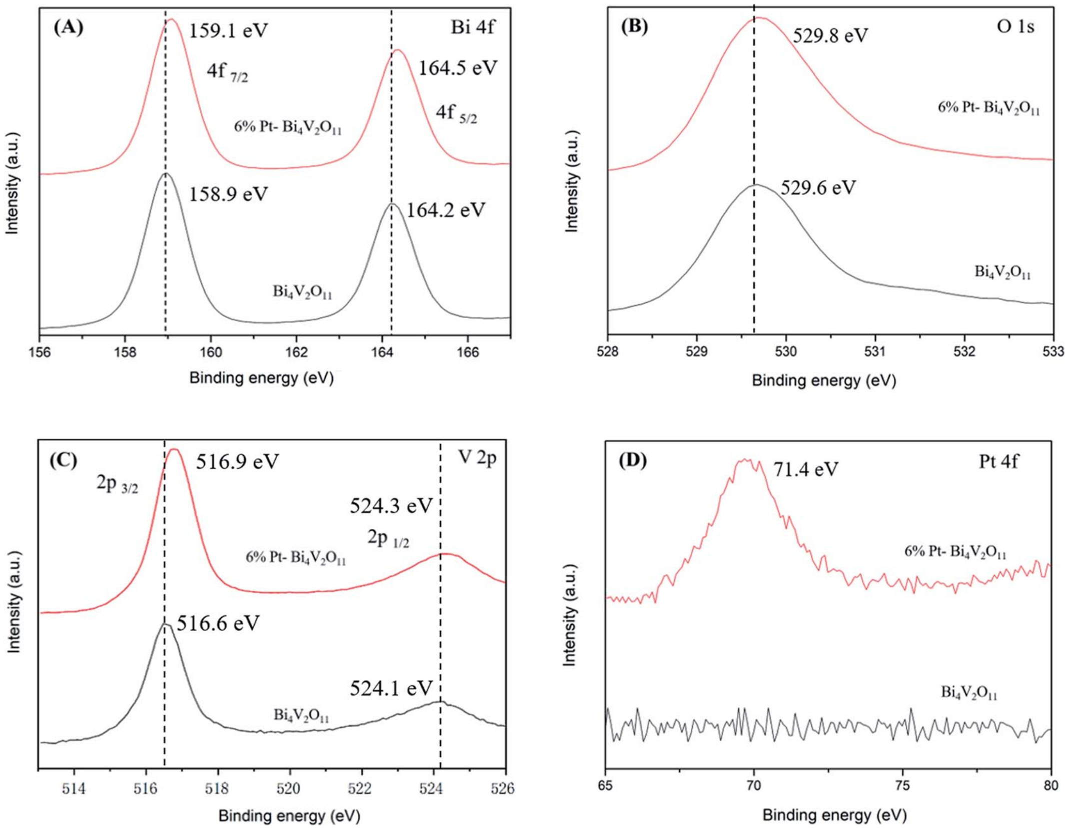

Fig. 4 XPS spectra of 6% Pt–$Bi_4V_2O_{11}$ and pristine $Bi_4V_2O_{11}$: Bi 4f (A), O 1s (B), V 2p (C) and Pt 4f (D).

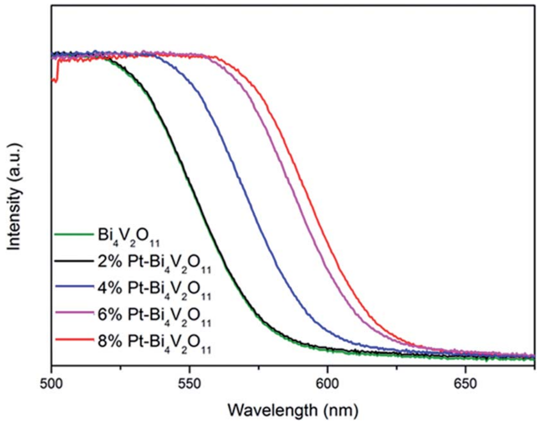

Fig. 5 UV-Vis DRS spectra of the $Bi_4V_2O_{11}$ and Pt–$Bi_4V_2O_{11}$ series samples.

photocatalytic performance. However, the carrier separation of the 8% Pt–$Bi_4V_2O_{11}$ sample was inhibited due to the excessively narrow band gap which greatly promoted the electron–hole pair recombination. In addition, because of the low loading content of Pt, the PL peak has no obvious deviation.

The main active component of 6% Pt–$Bi_4V_2O_{11}$ was studied by radical and hole trapping experiment. Three different quenching agents, isopropanol (IPA, 10 mM),[56] sodium oxalate ($Na_2C_2O_4$, 10 mM),[57] and benzoquinone (BQ, 1 mM),[58] were used as scavengers of hydroxyl radical ($^{\bullet}OH$), hole (h^+) and superoxide radical ($^{\bullet}O_2^-$), respectively. It could be observed in Fig. 7B that the catalytic properties of 6% Pt–$Bi_4V_2O_{11}$ were partially affected by IPA, indicating that hydroxyl radical ($^{\bullet}OH$) is one of the main radical during the photocatalytic procedure. After adding $Na_2C_2O_4$, the photocatalytic activity decreased obviously, this indicates that during the photodegradation of RhB, h^+ not only directly oxidizes degrade pollutants, but also generates $^{\bullet}OH$. The addition of BQ affected the photocatalytic activity, suggesting that the superoxide radical also take a big part in the photocatalytic procedure. The conduction band (CB) can be calculated according to the following equation:[59]

$$E_{CB} = \chi - E_e - \frac{1}{2}E_g$$

where χ is the electronegativity of the semiconductors, E_e is the energy of free electrons (4.5 eV), and E_g is the semiconductor band gap. The CB potential of $Bi_4V_2O_{11}$ was calculated to be 0.10 eV; this value is not negative enough for producing $^{\bullet}O_2^-$. It is worth noting that the quenching experiment results (Fig. 7B) showed that except for the h^+ and $^{\bullet}OH$, the superoxide radical ($^{\bullet}O_2^-$) also occupy a very important position in the photocatalytic procedure, this means that the Pt payload is able to efficiently use the electrons generated by the photoelectricity to generate the $^{\bullet}O_2^-$ radical.

In order to directly determine the main radicals of 6% Pt–$Bi_4V_2O_{11}$ in the photocatalytic process, the electron spin

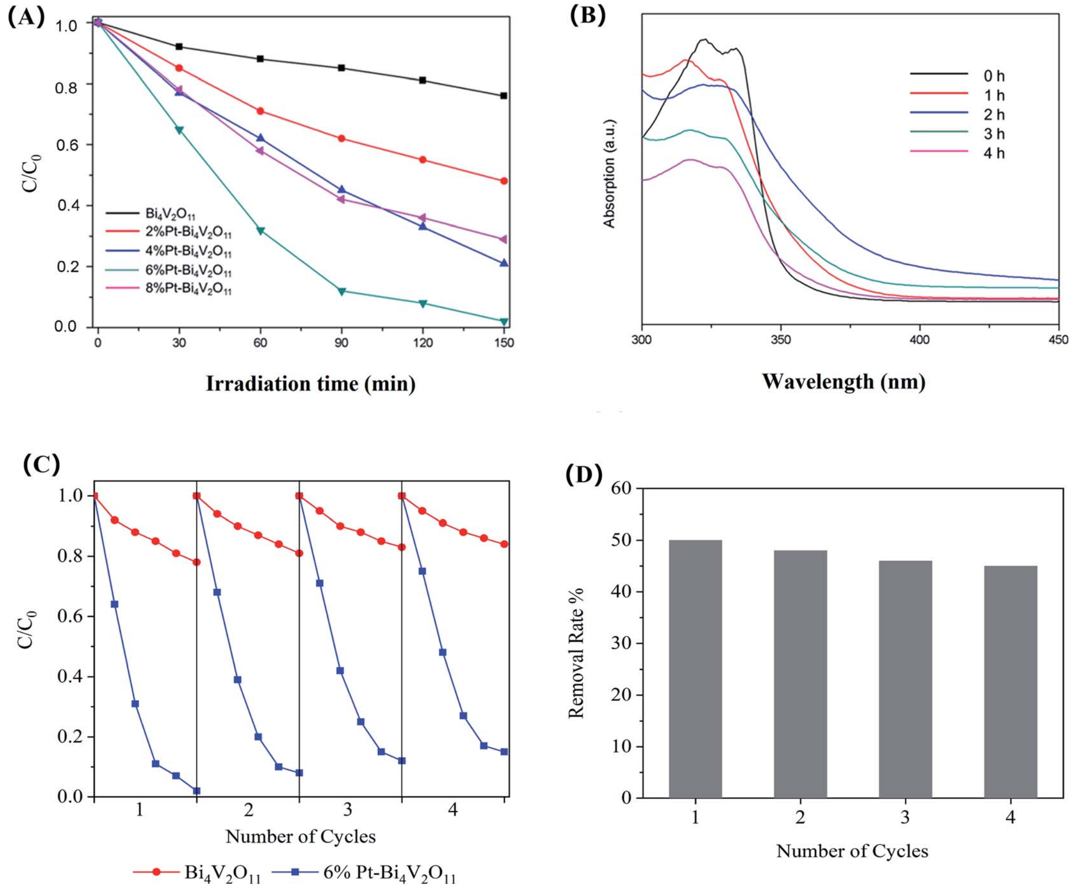

Fig. 6 Comparison of the degradation ration of RhB using pure $Bi_4V_2O_{11}$ and Pt–$Bi_4V_2O_{11}$ series samples (A), the degradation of ENR using 6% Pt–$Bi_4V_2O_{11}$ sample (B), cyclic photodegradation of RhB by 6% Pt–$Bi_4V_2O_{11}$ and $Bi_4V_2O_{11}$ sample (C), and the cyclic photodegradation rate of ENR by 6% Pt–$Bi_4V_2O_{11}$ (D).

resonance (ESR) technique was utilized to capture the $^{\bullet}O_2^-$ (A) and $^{\bullet}OH$ (B) signals under light irradiation and dark conditions. As shown in Fig. 7C and D, the 6% Pt–$Bi_4V_2O_{11}$ sample showed the obvious signals of both $^{\bullet}O_2^-$ and $^{\bullet}OH$ radicals after light irradiation. This result confirmed that Pt loaded $Bi_4V_2O_{11}$ could efficiently produce superoxide radicals and hydroxyl radicals during the photocatalytic process.

On the basis of the experimental and computational consequences, the possible photocatalytic mechanism of 6% Pt–$Bi_4V_2O_{11}$ under visible light illumination was put forward and the Fig. 8 shows the deduced photocatalytic procedure.

The detailed photocatalytic reaction process of 6% Pt–$Bi_4V_2O_{11}$ could be described as follows: photoelectrons (e^-) were transferred from VB to CB, and holes (h^+) were left in VB. For route (I), the adsorbed OH^- or H_2O were oxidized by the h^+ in VB and generated $^{\bullet}OH$, and the $^{\bullet}OH$ degraded organic pollutant. For route (II), part of the h^+ in VB could also oxidation the organic pollutants directly. Remarkably, the CB potential of pristine $Bi_4V_2O_{11}$ is much positive than $E(O_2/^{\bullet}O_2^-)$, and therefore, it is hard to produce $^{\bullet}O_2^-$ in the $Bi_4V_2O_{11}$ sample. However, the loading of Pt could not only efficiently facilitate the transfer of photogenerated charge carriers (Fig. 7A), but also directly utilize the electrons on the CB of $Bi_4V_2O_{11}$. Therefore, for route (III), the loaded Pt could react with the absorbed O_2 to produce $^{\bullet}O_2^-$, and degrade the organic pollutants. The following reactions clearly illustrate the degradation process:

$$6\%\ \text{Pt–Bi}_4\text{V}_2\text{O}_{11} + h\nu \rightarrow \text{electrons (CB)} + \text{holes (VB)}$$

$$\text{Electrons (CB)} \rightarrow \text{Pt} + O_2 \rightarrow {}^{\bullet}O_2^-$$

$$\text{Holes (VB)} + H_2O \rightarrow {}^{\bullet}OH + H^+$$

$$^{\bullet}OH + \text{organic waste} \rightarrow \text{carbon dioxide} + H_2O \qquad \text{(I)}$$

$$h_{VB}^{+} + \text{organic waste} \rightarrow \text{carbon dioxide} + H_2O \qquad \text{(II)}$$

$$^{\bullet}O_2^- + \text{organic waste} \rightarrow \text{carbon dioxide} + H_2O \qquad \text{(III)}$$

4. Conclusion

In summary, this study successfully synthesized $Bi_4V_2O_{11}$ and a series of efficient Pt–$Bi_4V_2O_{11}$ visible-light-driven photocatalysts. The photocatalytic performances of Pt–$Bi_4V_2O_{11}$ were

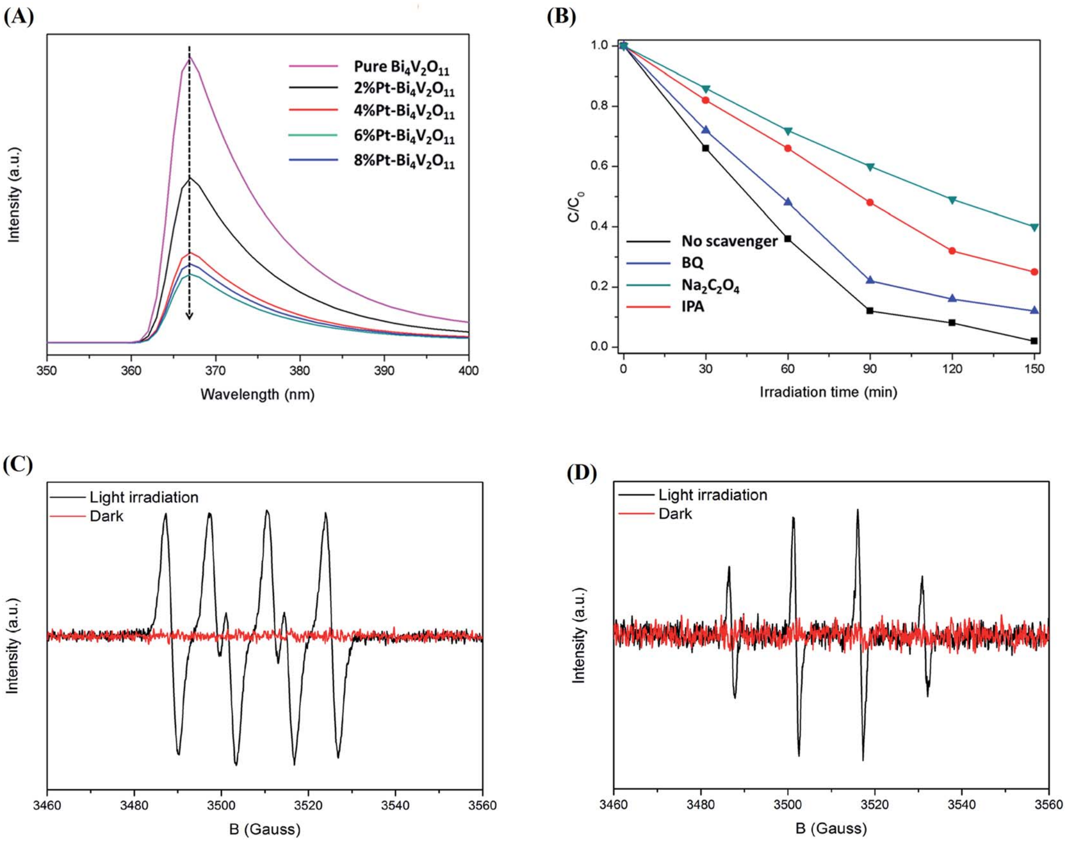

Fig. 7 Photoluminescence (PL) spectra of the pure $Bi_4V_2O_{11}$ and the Pt–$Bi_4V_2O_{11}$ series samples (A), the quenching experiment results of RhB degradation by 6% Pt–$Bi_4V_2O_{11}$ photocatalysts (B), ESR spectra of $^{\bullet}O_2^-$ (C) and $^{\bullet}OH$ (D) in the system of 6% Pt–$Bi_4V_2O_{11}$ under visible light irradiation and dark conditions.

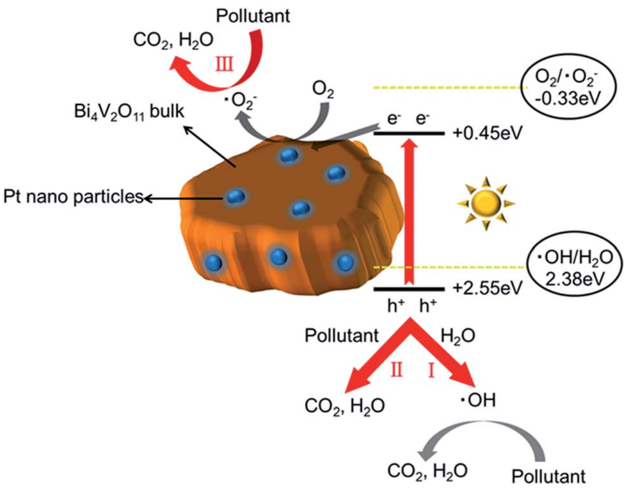

Fig. 8 Schematic illustration of the mechanism of the 6% Pt–$Bi_4V_2O_{11}$ photocatalyst activity under visible light irradiation.

obviously enhanced compared with pristine $Bi_4V_2O_{11}$, and 6% Pt–$Bi_4V_2O_{11}$ exhibited the highest photocatalytic activity. The results of UV-DRS and the PL spectra illustrated that the improvement of photocatalytic performance was because of the enhancement of light absorption range and the facilitation of transmission of charge carriers at the same time, which confirmed the hypothesis of loading appropriate noble metal could improve these two contradictory factors. Notably, the quenching experiments and ESR spectra revealed that other than the h^+ and $^{\bullet}OH$, abundant $^{\bullet}O_2^-$ was produced in the Pt–$Bi_4V_2O_{11}$ system, which were not observed in previous studies of $Bi_4V_2O_{11}$ based photocatalysts. Moreover, the mechanism of producing additional $^{\bullet}O_2^-$ was creatively proposed, which might be resulted from the loading of Pt could directly reduce the absorbed O_2, and generate $^{\bullet}O_2^-$ to enhance the photocatalytic performance. This study not only provided a novel visible-light-driven photocatalytic system for both organic dyes and antibiotics, but also put forward a promising strategy for producing additional radicals, which could enhance the photocatalytic performance in other applications such as CO_2 reduction and hydrogen production.

Conflicts of interest

There are no conflicts to declare.

Acknowledgements

This work was jointly supported by the National Key R&D Program of China (No. 2016YFC0700600 and 2016YFC0700901), the National Natural Science Foundation of China (No. 21878018 and 21906006), and the Fundamental Research Funds for the Central Universities (No. FRF-IDRY-19-026, FRF-MP-19-012 and FRF-TP-20-018A2). The authors would like to thank Shiyanjia lab (http://www.shiyanjia.com) for the BET and XPS analysis.

References

1 W. Wang, J. Fang, S. Shao, M. Lai and C. Lu, *Appl. Catal., B*, 2017, **217**, 57–64.
2 Y. Zhao, L. Zhu, W. Li, J. Liu, X. Liu and K. Huang, *J. Mol. Liq.*, 2019, **293**, 111516.
3 Z. L. Cheng, Y. X. Li and Z. Liu, *Ecotoxicol. Environ. Saf.*, 2018, **148**, 585–592.
4 M. Danish, W. A. Khanday, R. Hashim, N. S. B. Sulaiman, M. N. Akhtar and M. Nizami, *Ecotoxicol. Environ. Saf.*, 2017, **139**, 280–290.
5 H. Zeng, M. Gao, T. Shen and F. Ding, *Colloids Surf., A*, 2018, **555**, 746–753.
6 Y. Zhao, W. Li, Z. Liu, J. Liu, L. Zhu, X. Liu and K. Huang, *ACS Sustainable Chem. Eng.*, 2018, **6**, 15264–15272.
7 X. J. Wen, C. G. Niu, L. Zhang, C. Liang and G. M. Zeng, *Appl. Catal., B*, 2018, **221**, 701–714.
8 H. Yu, L. Jiang, H. Wang, B. Huang, X. Yuan, J. Huang, J. Zhang and G. Zeng, *Small*, 2019, **15**, e1901008.
9 H. Wang, C. Qian, J. Liu, Y. Zeng, D. Wang, W. Zhou, L. Gu, H. Wu, G. Liu and Y. Zhao, *J. Am. Chem. Soc.*, 2020, **142**, 4862–4871.
10 S. Chandrasekaran, C. Bowen, P. Zhang, Z. Li, Q. Yuan, X. Ren and L. Deng, *J. Mater. Chem. A*, 2018, **6**, 11078–11104.
11 S. Kundu and A. Patra, *Chem. Rev.*, 2017, **117**, 712–757.
12 X. Y. Kong, W. Q. Lee, A. R. Mohamed and S.-P. Chai, *Chem. Eng. J.*, 2019, **372**, 1183–1193.
13 S. Ijaz, M. F. Ehsan, M. N. Ashiq, N. Karamat and T. He, *Appl. Surf. Sci.*, 2016, **390**, 550–559.
14 X. An, C. Hu, H. Liu and J. Qu, *J. Mater. Chem. A*, 2017, **5**, 24989–24994.
15 Y. Hu, X. Hao, Z. Cui, J. Zhou, S. Chu, Y. Wang and Z. Zou, *Appl. Catal., B*, 2020, **260**, 118131.
16 J. Liu, Y. Yu, R. Qi, C. Cao, X. Liu, Y. Zheng and W. Song, *Appl. Catal., B*, 2019, **244**, 459–464.
17 C. Lv, G. Chen, J. Sun, Y. Zhou, S. Fan and C. Zhang, *Appl. Catal., B*, 2015, **179**, 54–60.
18 K. Deng, Z. Hou, X. Deng, P. Yang, C. Li and J. Lin, *Adv. Funct. Mater.*, 2015, **25**, 7280–7290.
19 H. Gu, C. Guo, S. Zhang, L. Bi, T. Li, T. Sun and S. Liu, *ACS Nano*, 2018, **12**, 559–567.
20 S. Ning, L. Ding, Z. Lin, Q. Lin, H. Zhang, H. Lin, J. Long and X. Wang, *Appl. Catal., B*, 2016, **185**, 203–212.
21 W. Xie, W. Hu, L. L. Zou and D. H. Bao, *Ceram. Int.*, 2015, **41**, S265–S273.
22 Y. Bai, L. Ye, T. Chen, L. Wang, X. Shi, X. Zhang and D. Chen, *ACS Appl. Mater. Interfaces*, 2016, **8**, 27661–27668.
23 J. Song, L. Zhang, J. Yang, J. S. Hu and X. H. Huang, *J. Alloys Compd.*, 2018, **735**, 660–667.
24 X. Jin, L. Ye, H. Wang, Y. Su, H. Xie, Z. Zhong and H. Zhang, *Appl. Catal., B*, 2015, **165**, 668–675.
25 C. Y. Wang, X. Zhang, H. B. Qiu, G. X. Huang and H. Q. Yu, *Appl. Catal., B*, 2017, **205**, 615–623.
26 D. Liu, W. Yao, J. Wang, Y. Liu, M. Zhang and Y. Zhu, *Appl. Catal., B*, 2015, **172**, 100–107.
27 C. Lv, G. Chen, X. Zhou, C. Zhang, Z. Wang, B. Zhao and D. Li, *ACS Appl. Mater. Interfaces*, 2017, **9**, 23748–23755.
28 C. Lv, G. Chen, J. Sun and Y. Zhou, *Inorg. Chem.*, 2016, **55**, 4782–4789.
29 X. J. Wen, L. Qian, X. X. Lv, J. Sun, J. Guo, Z. H. Fei and C. G. Niu, *J. Hazard. Mater.*, 2020, **385**, 121508.
30 X. Chen, J. Liu, H. Wang, Y. Ding, Y. Sun and H. Yan, *J. Mater. Chem. A*, 2013, **1**, 877–883.
31 X. Liu, Y. Zhu, W. Li, F. Wang, H. Li, C. Ren and Y. Zhao, *Appl. Surf. Sci.*, 2018, **458**, 1–9.
32 X.-l. Li, X.-j. Wang, J.-y. Zhu, Y.-p. Li, J. Zhao and F.-t. Li, *Chem. Eng. J.*, 2018, **353**, 15–24.
33 A. P. Devi, D. K. Padhi, P. M. Mishra and A. K. Behera, *J. Environ. Chem. Eng.*, 2020, 104778, DOI: 10.1016/j.jece.2020.104778.
34 P. He, T. Mao, A. Wang, Y. Yin, J. Shen, H. Chen and P. Zhang, *RSC Adv.*, 2020, **10**, 26067–26077.
35 B. Quan, W. Liu, Y. Liu, Y. Zheng, G. Yang and G. Ji, *J. Colloid Interface Sci.*, 2016, **481**, 13–19.
36 S. Ma, Y. Deng, J. Xie, K. He, W. Liu, X. Chen and X. Li, *Appl. Catal., B*, 2018, **227**, 218–228.
37 X. Rong, F. Qiu, J. Yan, H. Zhao, X. Zhu and D. Yang, *RSC Adv.*, 2015, **5**, 24944–24952.
38 X. Liu, Y. Su, J. Lang, Z. Chai and X. Wang, *J. Alloys Compd.*, 2017, **695**, 60–69.
39 Y. J. Yuan, H. W. Lu, Z. T. Yu and Z. G. Zou, *ChemSusChem*, 2015, **8**, 4113–4127.
40 X. Zhao, Z. Duan and L. Chen, *Ind. Eng. Chem. Res.*, 2019, **58**, 10402–10409.
41 Z. Yan, Z. Xu, L. Yue, L. Shi and L. Huang, *Chin. J. Catal.*, 2018, **39**, 1919–1928.
42 L. Zeng, Z. Lu, M. Li, J. Yang, W. Song, D. Zeng and C. Xie, *Appl. Catal., B*, 2016, **183**, 308–316.
43 J. Di, J. Xia, M. Ji, H. Li, H. Xu, H. Li and R. Chen, *Nanoscale*, 2015, **7**, 11433–11443.
44 L. Li, Y. Li, H. Wang, S. Liu and J. J. Bao, *Colloids Surf., A*, 2019, **570**, 322–330.
45 Z. Guo, J. Zhou, L. Zhu and Z. Sun, *J. Mater. Chem. A*, 2016, **4**, 11446–11452.
46 V. S. Bystrov, C. Piccirillo, D. M. Tobaldi, P. M. L. Castro, J. Coutinho, S. Kopyl and R. C. Pullar, *Appl. Catal., B*, 2016, **196**, 100–107.
47 F. Sun, S. Tan, H. Zhang, Z. Xing, R. Yang, B. Mei and Z. Jiang, *J. Colloid Interface Sci.*, 2018, **531**, 119–125.
48 A. Younis, D. Chu, Y. V. Kaneti and S. Li, *Nanoscale*, 2016, **8**, 378–387.
49 M. Xiao, Z. Wang, B. Luo, S. Wang and L. Wang, *Appl. Catal., B*, 2019, **246**, 195–201.
50 F. K. Naqvi, M. Faraz, S. Beg and N. Khare, *ACS Omega*, 2018, **3**, 11300–11306.

51 H. Wang, Y. Wu, M. Feng, W. Tu, T. Xiao, T. Xiong, H. Ang, X. Yuan and J. W. Chew, *Water Res.*, 2018, **144**, 215–225.

52 Y. Hong, Y. Jiang, C. Li, W. Fan, X. Yan, M. Yan and W. Shi, *Appl. Catal., B*, 2016, **180**, 663–673.

53 M. Ji, R. Chen, J. Di, Y. Liu, K. Li, Z. Chen, J. Xia and H. Li, *J. Colloid Interface Sci.*, 2019, **533**, 612–620.

54 N. Alarcos, B. Cohen, M. Ziolek and A. Douhal, *Chem. Rev.*, 2017, **117**, 13639–13720.

55 B. Chai and X. Wang, *RSC Adv.*, 2015, **5**, 7589–7596.

56 J. Tan, X. Wang, W. Hou, X. Zhang, L. Liu, J. Ye and D. Wang, *J. Alloys Compd.*, 2019, **792**, 918–927.

57 D. Wu, B. Wang, W. Wang, T. An, G. Li, T. W. Ng, H. Y. Yip, C. Xiong, H. K. Lee and P. K. Wong, *J. Mater. Chem. A*, 2015, **3**, 15148–15155.

58 A. G. Mojarrad and S. Zakavi, *RSC Adv.*, 2016, **6**, 100931–100938.

59 F. Chen, Q. Yang, X. Li, D. Wang, Y. Zhong, J. Zhao, Y. Deng, C. Niu and G. Zeng, *Catal. Commun.*, 2016, **84**, 137–141.